Cryogenic Second-Harmonic Generation in Periodically Poled Lithium Niobate Waveguides

Moritz Bartnick,[1,*] Matteo Santandrea,[2] Jan Philipp Höpker,[1] Frederik Thiele,[1] Raimund Ricken,[2] Viktor Quiring,[2] Christof Eigner,[2] Harald Herrmann,[2] Christine Silberhorn,[2] and Tim J. Bartley[1]

[1] *Department of Physics, Mesoscopic Quantum Optics, Paderborn University, Warburger Strasse 100, Paderborn 33098, Germany*

[2] *Department of Physics, Integrated Quantum Optics, Paderborn University, Warburger Strasse 100, Paderborn 33098, Germany*

(Received 9 October 2020; revised 8 December 2020; accepted 4 January 2021; published 11 February 2021)

We demonstrate second-harmonic generation in a fiber-coupled periodically poled titanium in-diffused lithium niobate waveguide over the temperatures range from 292 to 4.4 K. We observe a reproducible shift in the phase-matched pump wavelength within the telecom band, which is at odds with the phase matching arising from existing models of the refractive indices in this temperature regime. We further investigate transient discontinuities while temperature cycling, which we attribute to the build-up and discharge of pyroelectric fields. Our results show that modifications of the Sellmeier coefficients for lithium niobate are required in the cryogenic temperature regime for our waveguides, but also establish titanium in-diffused waveguides in lithium niobate as a versatile nonlinear photonic integration platform compatible with cryogenic quantum technologies.

DOI: 10.1103/PhysRevApplied.15.024028

I. INTRODUCTION

Nonlinear optical phenomena are fundamental to light-matter interaction and have wide-ranging practical applications. The study of nonlinear optical effects at cryogenic temperatures is useful in both regards, since it is both interesting to explore the temperature dependence of material systems as well as develop applications that require a low-temperature environment in which to operate. As a pertinent example, low temperatures are required in quantum photonics for many single-emitter single-photon sources, as well as superconducting detectors. One approach to building scalable quantum photonics is to integrate these individual technologies in a nonlinear material platform such as lithium niobate. As such, it is therefore crucial to investigate and understand the underlying nonlinear phenomena at cryogenic temperatures [1], before one can build functional devices such as frequency converters and modulators that function under these conditions.

Of many candidate platforms for quantum photonic integration, titanium in-diffused waveguides in lithium niobate [2] offer several advantages if one wishes to build functional devices at low temperature. They exhibit a high second-order nonlinearity, which is required for efficient frequency conversion, heralded single-photon generation, and squeezed-state generation. Moreover, they have a large electro-optic coefficient, which enables high-speed electro-optic modulation of phase and polarization, as well as routing. Furthermore, these waveguides support two orthogonal polarization modes, which, together with periodic poling, enable a range of different nonlinear processes to be phase matched. In principle, all of these processes are compatible with cryogenic temperatures; in practice, the electro-optic and nonlinear properties must be investigated and understood before quantum-compatible devices can be constructed.

Investigations into low-temperature nonlinear optics in lithium niobate have been carried out in the context of terahertz generation [3,4], microwave transduction [5,6], and phase modulation [7–9]. Moreover, some studies of material parameters of bulk lithium niobate at cryogenic temperatures have been conducted [10,11]. However, low-temperature experiments using low-loss waveguide structures suitable for quantum technologies with periodically poled phase matching have been limited [12].

To address this, in this paper we report on type-II second-harmonic generation (SHG) in periodically poled titanium in-diffused lithium niobate waveguides, with pump wavelengths around 1.55 μm and at temperatures down to 4.4 K. We demonstrate how the phase matching of the nonlinear interaction changes with temperature and explore the temperature-dependent material effects in the nonlinear medium. We observe deviations from current models of the Sellmeier equations, as well as temperature-dependent dynamics attributable to the pyroelectric effect in lithium niobate. Our work presents cryogenic SHG in

*moritz.bartnick@uni-paderborn.de

integrated nonlinear optical waveguides in lithium niobate, which are fully compatible with, and have been extensively used for, quantum photonic technologies [13–15].

II. TEMPERATURE DEPENDENCE OF SECOND-HARMONIC GENERATION

The nonlinear interaction that we implement is type-II SHG, whereby two electromagnetic waves in orthogonally polarized waveguide modes and with equal wavelengths λ_p combine to produce a third wave with half the wavelength, $\lambda_p/2$. The power of the generated second-harmonic light P_{SHG} depends on the effective second-order susceptibility-tensor element d_{eff}, as well as the phase mismatch of the interacting fields $\Delta\beta$ and the sample length L, and scales as [16]

$$P_{\mathrm{SHG}} \propto d_{\mathrm{eff}}^2 \,\mathrm{sinc}^2\left(\frac{\Delta\beta L}{2}\right). \tag{1}$$

While other configurations would enable a stronger interaction (e.g., type-0 phase matching exploits the large d_{33} element), we choose type-II phase matching to gain an insight into other nonlinear processes that use d_{13}, such as degenerate parametric down-conversion in orthogonal polarization modes [14].

From Eq. 1, maximal conversion is achieved when $\Delta\beta = 0$, which occurs at the phase-matched wavelength $\bar{\lambda}_p$. For our process, the phase mismatch can be expressed by

$$\frac{\Delta\beta}{2\pi} = \frac{2n_{\mathrm{TE}}\left(\frac{\lambda_p}{2}, T\right) - n_{\mathrm{TM}}(\lambda_p, T) - n_{\mathrm{TE}}(\lambda_p, T)}{\lambda_p} - \frac{1}{\Lambda(T)}, \tag{2}$$

where T designates the waveguide temperature and $\Lambda(T)$ is the poling period. The temperature dependence of $\Delta\beta$ arises due to thermal expansion of the poling period, as well as the temperature-dependent effective refractive indices of the interacting waves $n_{\mathrm{TE}}(\lambda_p/2, T)$, $n_{\mathrm{TM}}(\lambda_p, T)$, and $n_{\mathrm{TE}}(\lambda_p, T)$. Above 300 K, empirical Sellmeier relations for the refractive indices of congruent lithium niobate are known [17,18] (for more details, see Appendix A). In our experiment, we explore the behavior of the phase-matching relation in Eq. (2) below 300 K.

III. EXPERIMENTAL SETUP AND RESULTS

The sample is fabricated by in-diffusing a titanium strip of width 7 μm and height 80 nm into a 25-mm-long z-cut congruently grown lithium niobate chip. Using the electric-field-poling method [19], the waveguide is poled with a period of $\Lambda = 9.12$ μm, such that at room temperature, type-II SHG is phase matched for a pump wavelength in the telecom C band. To enable robust low-temperature operation, the chip is fiber coupled ("pigtailed") by gluing optical single-mode fibers to the waveguide end facets [14,15].

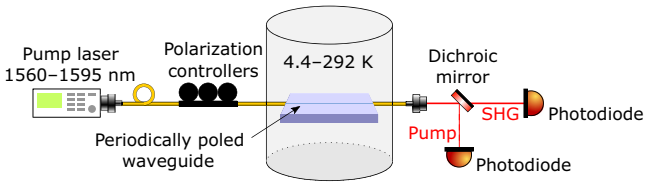

FIG. 1. The experimental setup to measure SHG spectra from a fiber-pigtailed waveguide sample inside a cryostat. All other components are at room temperature. For details, see the text.

For the low-temperature measurements, the lithium niobate chip is placed inside a Gifford McMahon cryocooler and the pigtailed fibers are spliced to optical fiber feedthroughs (see Fig. 1). We pump the nonlinear waveguide with a tunable narrow-band cw infrared laser (FWHM $\ll$ 1 pm). At the feedthrough into the cryostat, a total pump power of 17.5 mW is incident and we set the waveguide input polarization such that the SHG signal is maximized. The pump and second-harmonic light are coupled out and split by a dichroic mirror. We measure the SHG power and pump transmission with amplified photodiodes. During temperature cycling between 4.4 and 292 K, the transmission varies between 17% and 44% due to thermal contractions causing misalignment of the waveguide-to-fiber interconnections. Nevertheless, SHG is clearly observed throughout the entire temperature range. Moreover, because we observe a constant sample transmission at the lowest temperature of 4.4 K, we assume that photorefraction plays a negligible role in the measurement time scales involved in our experiment.

A. Cryogenic SHG spectra

To measure the effects of temperature change on the SHG, the sample is cooled down to 4.4 K over about 15 h and subsequently warmed up over about 20 h. During temperature cycling, we continuously measure SHG spectra by sweeping the pump wavelength between 1560 nm and 1595 nm in steps of 0.1 nm, over a time period of 260 s. This corresponds to a maximum temperature variation of 2 K within one spectrum. Figure 2(a) shows an example of monitoring of the spectra between 4.4 and 292 K. Two main peaks separated by approximately 22 nm arise due to SHG in both the fundamental mode and a higher-order mode. The central wavelength of the SHG peak of both modes shifts toward longer wavelengths with decreasing temperature.

In Fig. 2(b), the phase-matched wavelength of the fundamental mode is plotted as a function of the temperature for four separate measurements, as well as its expected behavior due to the extrapolated Sellmeier equations [17,

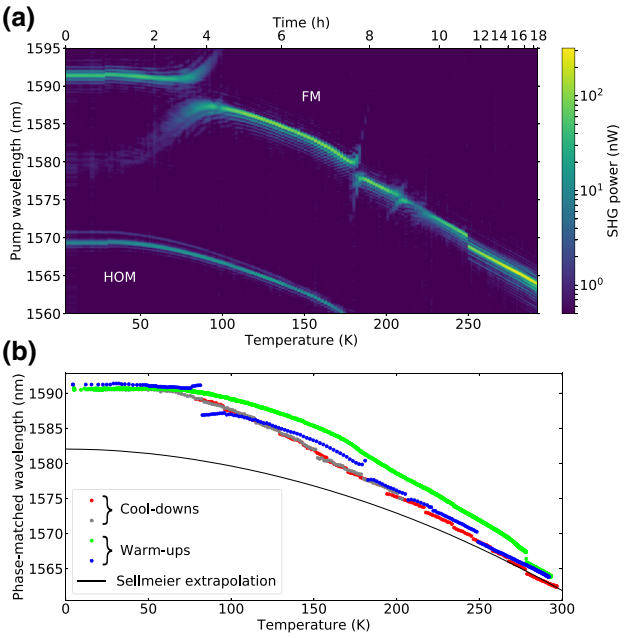

FIG. 2. (a) The measured SHG power dependent on the pump wavelength and temperature, in the fundamental (FM) and higher-order (HOM) mode. (b) The phase-matched pump wavelength $\bar{\lambda}_p$ of the fundamental mode as a function of the temperature. The curve calculated from the extrapolated Sellmeier equations (black line) predicts a smaller wavelength shift than that measured in two separate temperature cycles (red and gray dots, cool-downs; blue and green dots, warm-ups).

18], modified for the waveguide geometry (for details, see Appendix A). For all measurement runs, a shift in the phase-matched wavelength could be consistently reproduced, from (1562.7 ± 1.7) nm at 292 K to (1590.3 ± 2.5) nm at 4.4 K. The experimentally observed increase in the phase-matched wavelength is significantly larger than the shift to 1582 nm expected from extrapolating the Sellmeier equations, motivating further investigation in this temperature regime.

B. Conversion efficiency

We clearly observe SHG throughout the entire temperature range. We estimate an internal conversion efficiency varying between $2.4 \times 10^{-4}\%\mathrm{W}^{-1}\mathrm{cm}^{-2}$ and $3.9\%\mathrm{W}^{-1}\mathrm{cm}^{-2}$ at 4.4 K and $2.3 \times 10^{-3}\%\mathrm{W}^{-1}\mathrm{cm}^{-2}$ and $5.9\%\mathrm{W}^{-1}\mathrm{cm}^{-2}$ at 292 K. The large uncertainty arises from determining the outcoupling efficiency of the second harmonic; further details on this calculation are provided in Appendix B. Figure 3 shows the temperature-dependent conversion efficiency for the SHG process which we estimate for the measurement shown in Fig. 2(a).

C. Transient spectral dynamics

On top of an underlying reproducible trend in the phase-matched wavelength, we observe significant dynamics in

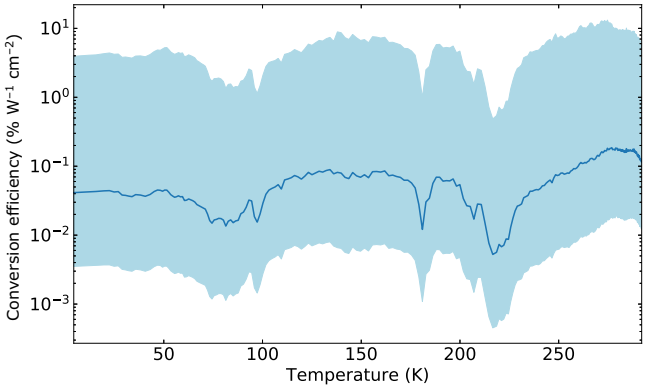

FIG. 3. The estimated internal conversion efficiency as a function of the temperature (dark blue line), with the corresponding uncertainty interval (light blue area).

the SHG spectra, occurring on different time scales and at random temperatures, across the four measurements (see Fig. 2). In Fig. 2(a), at least three discontinuities in the phase-matched wavelength can be identified, located around 85 K, at 180 K, and at 249 K. Between 67 and 92 K, a discontinuity exists over a time scale of 2.5 h, whereas at 180 K this takes place over 10 min, and at 249 K, this occurs between obtaining two successive spectra, < 260 s. Furthermore, experimental data showing even faster discontinuities can be seen in Fig. 2(b) and further evidence of this occurs in the additional data shown in Appendix C. Since the cooling rate is roughly constant across the relevant temperature range from 50 to 250 K, the different time scales of these phenomena point toward temperature-dependent underlying physical processes that modify the phase-matching conditions. Moreover, the spectra shown in Fig. 2(a) might suggest that such perturbations of the phase-matching spectra are mode-dependent, since no discontinuities are observed in the higher-order mode, while they are clearly present in the fundamental mode. However, further experiments demonstrate correlated discontinuities affecting both modes, details of which are provided in Appendix C.

IV. REGRESSION ANALYSIS OF SHG SPECTRA

To model the cryogenic SHG spectra, we consider a spatially dependent phase-matching relation along the waveguide. For this, we proceed in two steps. First, we use our experimental data to correct the temperature dependency of the extrapolated Sellmeier equations. Second, we determine distorted SHG spectra based on perturbations in the phase mismatch along the waveguide.

A. Temperature-dependent phase-mismatch correction

The unperturbed phase mismatch for our type-II SHG process is given by

$$\Delta\beta = 2\pi\left[\frac{\Delta n(\lambda_p, T)}{\lambda_p} - \frac{1}{\Lambda(T)}\right], \tag{3}$$

depending on the linear combination of (effective) refractive indices

$$\Delta n(\lambda_p, T) = 2n_{\mathrm{TE}}\left(\frac{\lambda_p}{2}, T\right) - n_{\mathrm{TM}}(\lambda_p, T) - n_{\mathrm{TE}}(\lambda_p, T). \tag{4}$$

The linear combination $\Delta n(\lambda_p, T)$ can be approximated based on the extrapolation of the refractive indices given in Appendix A. However, we observe that the shift in the phase-matched wavelength is greater than that predicted according to the extrapolation. Hence we determine a corrected linear combination $\Delta n^{\mathrm{corr}}(\lambda_p, T)$ by adding a corrective function $a(T)$ to the extrapolated linear combination $\Delta n^{\mathrm{extrp}}$:

$$\Delta n^{\mathrm{corr}}(\lambda_p, T) = \Delta n^{\mathrm{extrp}} + a(T). \tag{5}$$

At every temperature T, we determine $a(T)$ from our measured cryogenic SHG spectra, based on the average phase-matched pump wavelength $\bar{\lambda}_p$ at which the SHG signal is maximal. At the phase-matched wavelength, $\Delta\beta = 0$ and we can calculate $a(T)$ from

$$\frac{\Delta n^{\mathrm{extrp}}(\bar{\lambda}_p, T) + a(T)}{\bar{\lambda}_p} - \frac{1}{\Lambda(T)} = 0. \tag{6}$$

From this, we calculate the corrected phase mismatch $\Delta\beta^{\mathrm{corr}}$, arising from the corrected linear combination $\Delta n^{\mathrm{corr}}(\lambda_p, T)$:

$$\Delta\beta^{\mathrm{corr}} = 2\pi\left[\frac{\Delta n^{\mathrm{corr}}(\lambda_p, T)}{\lambda_p} - \frac{1}{\Lambda(T)}\right]. \tag{7}$$

B. Locally perturbed phase matching

To describe SHG spectra deviating from the ideal sinc-squared shape, we introduce local perturbations in the corrected phase mismatch along the waveguide:

$$\Delta\beta^{\mathrm{corr}}(\lambda_p) \rightarrow \Delta\beta^{\mathrm{corr}}(\lambda_p) + \delta\beta(x). \tag{8}$$

From such perturbations, the shape of the SHG spectrum can be theoretically calculated by [21]

$$P_{\mathrm{theo}}(\lambda_p) \propto \left|\int_0^L e^{-i\Delta\beta^{\mathrm{corr}}(\lambda_p)x} e^{-i\int_0^x \delta\beta(x')dx'} dx\right|^2. \tag{9}$$

With a regression approach, we determine perturbations in the phase mismatch $\delta\beta(x)$ resulting in modeled normalized SHG spectra $p_{\mathrm{theo}}(\lambda_p)$ that fit the normalized experimental SHG spectra $p_{\mathrm{exp}}(\lambda_p)$. Since we consider SHG in the waveguide ground mode, the side peak due to SHG in the higher mode is cut off the experimental spectra.

For all SHG spectra $p_{\mathrm{exp}}(\lambda_p)$ measured at temperatures T, we determine a perturbation $\delta\beta(x)$ generating the respective intensity distribution. To do so, we approximate the perturbations by a step function consisting of seven equally broad plateaus of height c_i.

$$\delta\beta_{\mathrm{step}}(x, c_1, \ldots, c_7) = c_i \quad \text{for} \quad \frac{i-1}{7}L \le y < \frac{i}{7}L, \quad \text{where} \quad i = 1, \ldots, 7. \tag{10}$$

We choose seven steps as a trade-off between fitting quality and computational effort.

For each measured SHG spectrum, we fit an intensity distribution $p_{\mathrm{model}}(\lambda_p, L, c_1, \ldots, c_7)$ based on a seven-step perturbation $\delta\beta_{\mathrm{step}}(x, c_1, \ldots, c_7)$. We solve the integral in Eq. (9) using Simpson's method implemented in the PyNumericalPhasematchingv1.0b package [22]. The sample length is fitted once at $T = 4.4$ K and kept constant during the further analysis since perturbations along the waveguide have no influence on this parameter. The determined length is $L = 21.85$ mm, which can be interpreted as an effective length, being shorter than the actual sample length of 25 mm due to waveguide imperfections.

For each spectrum, we perform a two-step regression procedure with respect to the parameters $\{c_i\}$. In the first step, 10^3 spectra based on random regression parameters are simulated. In a second step, the best random guess $\{c_i\}_{\mathrm{init}}$ leading to the least residual sum of squares (RSS) is used as the initial point for a function regression with the Levenberg-Marquardt algorithm [23].

C. Regression results

Figure 4 shows three individual spectra (obtained at different temperatures) from Fig. 2 and their corresponding reconstructions. Our simple model matches the measured data remarkably accurately, for ideal spectra such as in Fig. 4(a) at 4.4 K, as well as the highly distorted profile in Fig. 4(b) at 85 K and the slightly asymmetric profile at 249 K in Fig. 4(c).

In Fig. 5(a), the determined perturbations $\delta\beta(x)$ along the waveguide are plotted as a function of the temperature T. The coefficient of determination R^2, plotted as a function of the temperature in Fig. 5(b), varies between 0.833 and 0.999. The impressive quality of the fits indicates that the waveguide does indeed undergo localized temperature-dependent perturbations.

We attribute the source of these perturbations to the complex interplay of several coupled effects including pyroelectricity, electro-optics, and piezoelectric strain [24,25] which influence the refractive indices. The build-up and subsequent relaxation dynamics that we observe

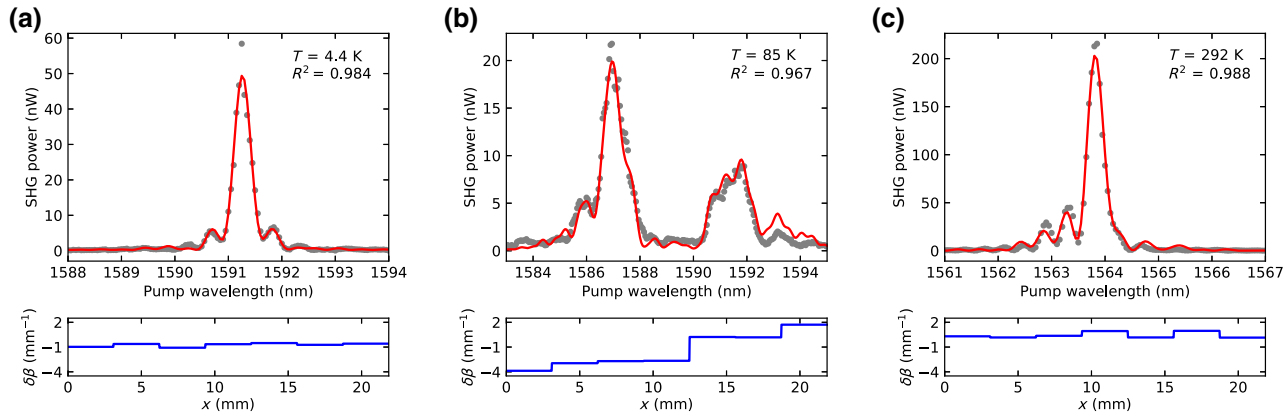

FIG. 4. Top: measured (gray) and fitted (red) SHG spectra at (a) 4.4 K, (b) 85 K, and (c) 292 K. Bottom: corresponding modeled local perturbations $\delta\beta(x)$ in the phase mismatch arising from the fitted spectra. The spectra and fits for all temperatures from 4.4 to 292 K are provided as a video in the Supplemental Material [20].

could be explained by the accumulation and discharge of pyroelectric fields. To support this hypothesis, we consider the magnitudes of these fields that arise during the temperature cycling of lithium niobate in vacuum.

Without discharging, from 4.4 to 292 K, we would expect an electric field build-up [26] of the order of $|\Delta E| = |\Delta P_s|/\epsilon_0 = 1.3\,\mathrm{MV\,mm^{-1}}$, where ϵ_0 is the electric field constant. Such fields, larger than the coercive field strength of $21\,\mathrm{kV\,mm^{-1}}$ [27], would likely be sufficient to affect the periodic poling irreversibly. This would result in partial erasing of the poling structure, corresponding to a permanent increase in the width of the SHG spectrum after temperature cycling, which is not observed. In fact, at both 4.4 and 292 K, we record SHG spectra with the same spectral width of 0.3 nm FWHM [see, e.g., Figs. 4(a) and 4(c)]. Therefore, we deduce that there must be some discharge of the field during temperature cycling.

Because our sample is in an evacuated cryostat, there exists no efficient pathway for electric charges to dissipate (e.g., via atmospheric ions). Furthermore, the long time scales of the dynamics, particularly at cold temperatures, suggest that reduced charge mobility at low temperatures [28,29] plays a role in the discharge dynamics. This hints at discharging pathways through the lithium niobate itself. However, further data on the electrical properties of lithium niobate under these conditions are needed to corroborate this hypothesis.

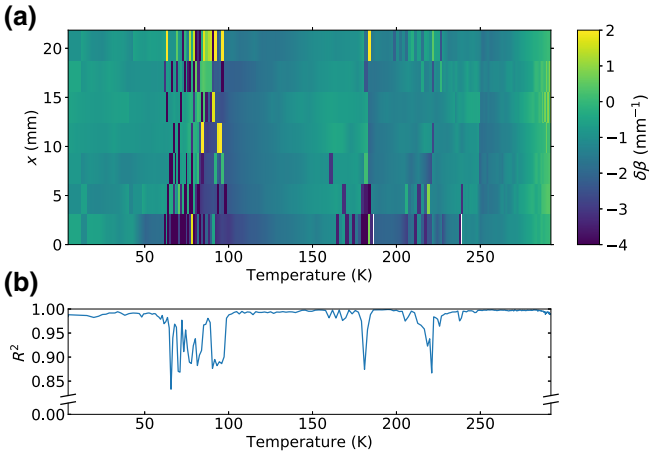

FIG. 5. The fitted perturbations $\delta\beta$ along the waveguide in the x direction as a function of the temperature T. The coefficient of determination R^2 indicates that the modeled SHG spectra agree very well with the measured SHG spectra, exhibiting a single SHG peak. Spectra with double phase matching could be modeled by refractive index perturbations as well.

V. CONCLUSION

In summary, we demonstrate type-II SHG down to 4.4 K in a periodically poled titanium in-diffused lithium niobate waveguide. We quantify a shift in the phase-matched wavelength, which suggests that the Sellmeier equations for this system should be modified in this temperature range. Further, we observe SHG spectra deviating from the ideal sinc-squared shape. We develop a model that accurately describes the shape of the SHG spectra by localized changes to the propagation conditions along the nonlinear waveguide. Our modeling is a strong indicator that the waveguide properties undergo local perturbations, which we attribute to the accumulation and discharge of pyroelectric fields over different time scales. Overall, our analysis provides an indirect way to access the dynamics occurring within the waveguide itself.

For some experiments, it may be advantageous to mitigate the accumulation of pyroelectric charges. However, below 50 K, the phase-matched wavelength is consistently reproducible across measurement runs, which indicates that the observed transient dynamics play a minimal role

for quasi-phase-matched type-II SHG at low temperature. In addition to investigating the phase matching, it may be interesting in future to study the behavior of the nonlinear coefficient itself under cryogenic conditions. Our experiment is not sufficiently sensitive to changes in this quantity; further experiments that are independent of the waveguide coupling efficiency would be required to extract this. Nevertheless, our cryogenic compatible packaging and characterization allows the phase-matching dynamics of many more nonlinear optical phenomena to be studied at low temperature.

ACKNOWLEDGMENTS

This project is supported by the German Federal Ministry of Education and Research (BMBF) under the "Quantum Futur" Program, Project No. 13N14911, the European Union (EU) via the EU quantum flagship project "Affordable Quantum Communication for Everyone" (UNIQORN) (Grant No. 820474), and the Deutsche Forschungsgemeinschaft (DFG).

APPENDIX A: TEMPERATURE-DEPENDENT REFRACTIVE INDICES BASED ON MODIFIED SELLMEIER EQUATIONS

In order to anticipate the temperature dependence of our SHG process, we calculate temperature- and wavelength-dependent effective refractive indices using a commercial mode-solving software package based on the finite-element method (RSoft FemSIM [30]). The effective refractive indices are determined from refractive-index cross sections $n_{o,e}(y,z,\lambda,T)$, calculated from the bulk refractive indices $n_{o,\mathrm{bulk}}(\lambda,T)$ and $n_{e,\mathrm{bulk}}(\lambda,T)$, locally increased by $\delta n_{o,e}(\lambda,c)$ due to the in-diffusion of titanium:

$$\begin{aligned} n_o(y,z,\lambda,T) &= n_{o,\mathrm{bulk}}(\lambda,T) + \delta n_o(\lambda,c), \\ n_e(y,z,\lambda,T) &= n_{e,\mathrm{bulk}}(\lambda,T) + \delta n_e(\lambda,c). \end{aligned} \tag{A1}$$

For the bulk refractive indices, we use empirical Sellmeier relations for temperatures above 300 K, which are extrapolated for our analysis into the regime of cryogenic temperatures. For the ordinary refractive index (for TE polarization), we use [17]

$$n^2_{o,\mathrm{bulk}} = A_1 + \frac{A_2 + B_1 H}{\lambda^2 - (A_3 + B_2 H)^2} + B_3 H - A_4 \lambda^2, \tag{A2}$$

with

$$H = (T - 24.5)(T + 570.5), \tag{A3}$$

where, by convention, λ is the numerical value of the wavelength in microns, T is the numerical value of the temperature in degrees Celsius, and A_1, A_2, A_3, A_4, B_1, B_2, and B_3 are dimensionless empirical constants, summarized in Table I. We follow the convention that the units of these constants are dimensionless.

TABLE I. The constants in the empirical Sellmeier relations.

Ordinary		Extraordinary	
A_1	4.9048	a_1	5.355 83
A_2	0.117 75	a_2	0.100 473
A_3	0.218 02	a_3	0.206 92
A_4	0.0271 53	a_4	100
B_1	2.2314×10^{-8}	a_5	11.349 27
B_2	-2.9671×10^{-8}	a_6	1.5334×10^{-2}
B_3	2.1429×10^{-8}	b_1	4.629×10^{-7}
		b_2	3.862×10^{-8}
		b_3	-0.89×10^{-8}
		b_4	2.657×10^{-5}

For the extraordinary refractive index (for TM polarization), we use [18]

$$n^2_{e,\mathrm{bulk}} = a_1 + b_1 h + \frac{a_2 + b_2 h}{\lambda^2 - (a_3 + b_3 h)^2} + \frac{a_4 + b_4 h}{\lambda^2 - a_5^2} - a_6 \lambda^2, \tag{A4}$$

with

$$h = (T - 24.5)(T + 570.82), \tag{A5}$$

where, as before, λ is the numerical value of the wavelength in microns, T is the numerical value of the temperature in degrees Celsius, and a_1, a_2, a_3, a_4, a_5, a_6, b_1, b_2, b_3, and b_4 empirical constants, summarized in Table I.

We assume that the spatial refractive-index increase due to the in-diffusion of titanium is independent of the temperature, depending only on the wavelength and the titanium concentration c. We quantify the spatial refractive index increase according to Ref. [31] by

$$\delta n_{o,e}(\lambda,c) = d_{o,e}(\lambda) f_{o,e}(c), \tag{A6}$$

where $d_{o,e}(\lambda)$ and $f_{o,e}(c)$ are empirical functions, given by

$$d_o(\lambda) = \frac{0.67\lambda^2}{\lambda^2 - 0.13}, \tag{A7}$$

$$d_e(\lambda) = \frac{0.839\lambda^2}{\lambda^2 - 0.0645}, \tag{A8}$$

$$f_o(c) = (Fc)^\gamma, \tag{A9}$$

and

$$f_e(c) = Ec, \tag{A10}$$

with $E = 1.2 \times 10^{-23}$ cm^3, $F = 1.3 \times 10^{-25}$ cm^3 and $\gamma = 0.55$. As before, λ is the numerical value of the wavelength in microns.

For the cross-section titanium concentration $c(z,y)$, we use the profile for an in-diffused titanium strip of thick-

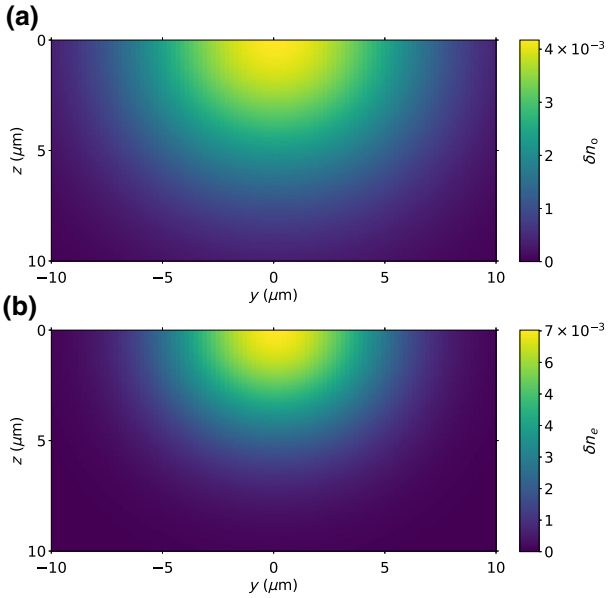

FIG. 6. The modeled increases in the (a) ordinary and (b) extraordinary refractive index of lithium niobate at $\lambda = 1.55\ \mu$m.

ness $\tau = 0.08\ \mu$m and $W = 7\ \mu$m, specified according to Ref. [31] by

$$c(z,y) = c_0 f(u) g(s), \tag{A11}$$

with

$$c_0 = \frac{\tau}{a D_y}, \tag{A12}$$

where $a = 1.57 \times 10^{-23}$ cm^3 is a constant parameter and D_y is the diffusion depth perpendicular to the crystal axis. The functions u and s are connected to the crystal coordinates y and z via

$$u = \frac{y}{D_y} \quad \text{and} \quad s = \frac{2z}{W}. \tag{A13}$$

The functions $f(u)$ and $g(s)$ are given by

$$f(u) = \exp(-u^2) \tag{A14}$$

and

$$g(s) = \frac{\operatorname{erf}\left[\left(\frac{W}{2D_z}\right)(1+s)\right] + \operatorname{erf}\left[\left(\frac{W}{2D_z}\right)(1-s)\right]}{2} \tag{A15}$$

and depend, furthermore, on the diffusion depth D_z along the crystal axis. The investigated waveguide is fabricated by in-diffusing the titanium stripe for 8.5 h at a temperature of 1060 °C, specifying the diffusion depths $D_y = 4.0\ \mu$m and $D_z = 3.7\ \mu$m determined by our commercial mode-solving software [30–32]. Figure 6 shows the resulting modeled cross-section refractive-index increases at 1.55 μm wavelength.

APPENDIX B: DETERMINATION OF THE CONVERSION EFFICIENCY

We define the internal conversion efficiency of our waveguide according to

$$\eta_{\mathrm{SHG}} = \frac{P'_{\mathrm{SHG}}}{P'^2_{\mathrm{pump}} L^2} \times 100\%, \tag{B1}$$

where $L = 2.5$ cm is the waveguide length and P'_{SHG} is the amount of SHG power generated with the phase-matched pump wavelength at the end of the waveguide (before outcoupling). $P'_{\mathrm{pump}} = \eta_{\mathrm{in}}^{(\mathrm{pump})} P_{\mathrm{pump}}$ denotes the portion of the pump power that is coupled from the input fiber into the waveguide.

Due to thermal contractions while temperature cycling, the incoupling efficiency $\eta_{\mathrm{in}}^{(\mathrm{pump})}$ as well as the outcoupling efficiencies $\eta_{\mathrm{out}}^{(\mathrm{SHG})}$ and $\eta_{\mathrm{out}}^{(\mathrm{pump})}$ of the second harmonic and the pump vary during the experiment. From our measurements, we know the pump power P_{pump} before incoupling and the SHG power after outcoupling $P_{\mathrm{SHG}} = \eta_{\mathrm{out}}^{(\mathrm{SHG})} P'_{\mathrm{SHG}}$. To determine the quantities P'_{pump} and P'_{SHG}, which are required to calculate the internal conversion efficiency η_{SHG}, we use the monitored sample transmission

$$T_{\mathrm{sample}} = \eta_{\mathrm{in}}^{(\mathrm{pump})} \eta_{\mathrm{out}}^{(\mathrm{pump})}. \tag{B2}$$

The uncertainty in the coupling efficiencies $\eta_{\mathrm{in}}^{(\mathrm{pump})}$ and $\eta_{\mathrm{out}}^{(\mathrm{pump})}$ causes the large uncertainty in the internal conversion efficiency, identified by the blue band in Fig. 3. More details on determining the uncertainty are provided in Appendix B.

To determine the conversion efficiency, it is necessary to measure the output coupling efficiency of the SHG light $\eta_{\mathrm{out}}^{(\mathrm{SHG})}$. Because $\eta_{\mathrm{out}}^{(\mathrm{SHG})}$ cannot be measured directly and may differ significantly from $\eta_{\mathrm{out}}^{(\mathrm{pump})}$ (which can be inferred), it is necessary to find the relationship between the coupling efficiencies for each wavelength. To do so, we model the mode overlap between the waveguide and the fiber at 775 nm and 1550 nm in the presence of lateral misalignment of the outcoupling pigtail. This yields that $\eta_{\mathrm{out}}^{(\mathrm{SHG})}$ is approximated by the function $f\,(\eta_{\mathrm{out}}^{(\mathrm{pump})})$ plotted in Fig. 7.

Under these assumptions, we quantify an upper and a lower bound on the internal conversion efficiency as a function of the temperature (see the light blue area in Fig. 3). To calculate the upper bound, we assume the best incoupling $\eta_{\mathrm{in}}^{(\mathrm{pump})} = 0.95$ (limited by the maximum mode overlap between the waveguide and the fiber without lateral displacement) and the worst outcoupling $\eta_{\mathrm{out}}^{(\mathrm{pump})} = T_{\mathrm{sample}}/0.95$, leading to

$$\eta_{\mathrm{SHG}}^{\mathrm{max}} = \frac{1}{f(T_{\mathrm{sample}}/0.95)0.95^2} \frac{P_{\mathrm{SHG}}}{P^2_{\mathrm{pump}} L^2} \times 100\%. \tag{B3}$$

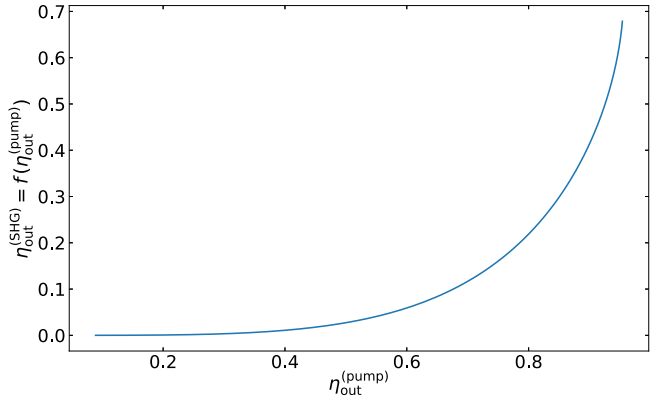

FIG. 7. A parametric plot showing the relationship between $\eta_{out}^{(pump)}$ and $\eta_{out}^{(SHG)}$, considering a lateral displacement of the outcoupling fiber. We calculate the mode overlap by varying the displacement from 0 to 15 μm in the vertical direction, perpendicular to the surface of the chip.

Moreover, we quantify the lower boundary of the internal conversion efficiency by the external conversion efficiency of our pigtailed waveguide, given by

$$\eta_{SHG}^{min} = \frac{P_{SHG}}{P_{pump}^2 L^2} \times 100\%. \tag{B4}$$

Between these limits, the dark blue line in Fig. 3 indicates the conversion efficiency estimated under the assumption of equal coupling at 1550 nm, i.e., $\eta_{in}^{(pump)} = \eta_{out}^{(pump)} = T_{sample}^{1/2}$, such that the conversion efficiency is assumed to be

$$\overline{\eta}_{SHG} = \frac{1}{f(T_{sample}^{1/2}) T_{sample}} \frac{P_{SHG}}{P_{pump}^2 L^2} \times 100\%. \tag{B5}$$

The resulting internal conversion efficiency is given by the dark blue line in Fig. 3. The large uncertainty interval arises from the modeled relationship between $\eta_{out}^{(SHG)}$ and $\eta_{out}^{(pump)}$, as well as the uncertainty in determining $\eta_{out}^{(pump)}$ itself.

APPENDIX C: FURTHER CRYOGENIC SHG SPECTRA

The monitored SHG spectra summarized in Fig. 2(b) are shown in Fig. 8. The SHG power is measured as a function of the wavelength and temperature across different temperature and wavelength ranges. Figures 8(a) and 8(b) show the transient dynamics in the SHG spectra, affecting SHG in the fundamental mode simultaneously with SHG in the higher-order mode.

For the data plotted in Fig. 8(c), the pump wavelength is swept over a 5-nm broad wavelength interval, centered dynamically around the phase-matched wavelength

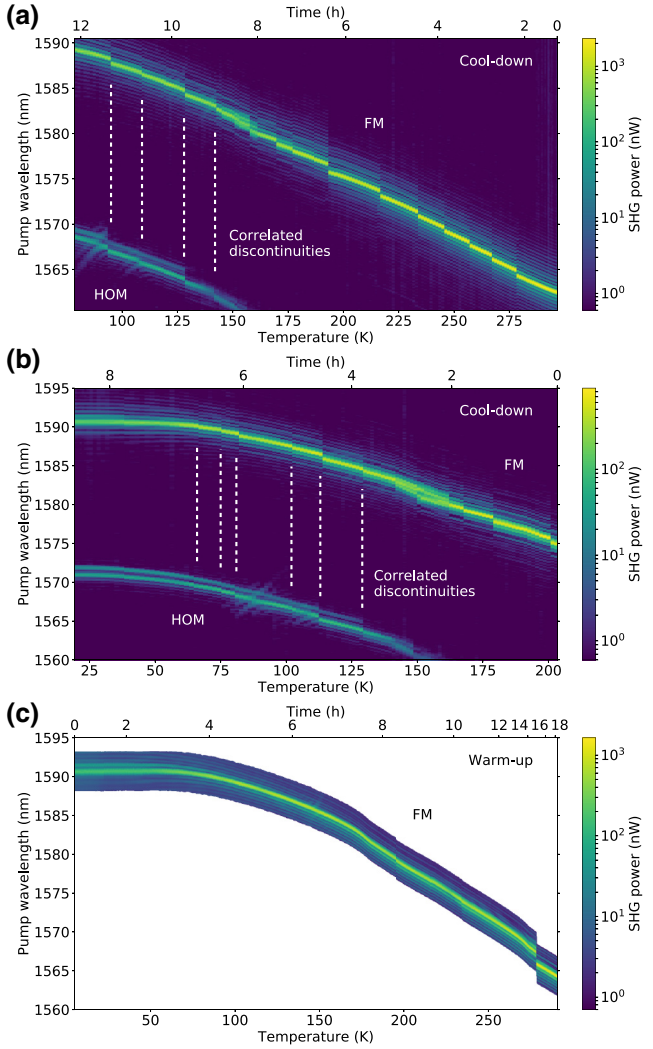

FIG. 8. The SHG power as a function of the pump wavelength and temperature, measured across different temperature and wavelength ranges. The spectra in (a) and (b) show strong correlation of the transient dynamics in the fundamental mode (FM) and the higher-order mode (HOM). For the measurement in (c), the timing resolution is enhanced by only monitoring SHG in the fundamental mode, resolving a jump in phase-matched wavelength occurring within the sweep of two wavelength increments. We provide an animated version of this data in the Supplemental Material [20].

of SHG in the fundamental mode during temperature cycling. This measurement approach allows us to resolve the discontinuity at 278 K and see that the SHG spectrum switches within the sweep of two wavelength increments, i.e., within less than 0.7 s.

[1] G. F. Sinclair, N. A. Tyler, D. Sahin, J. Barreto, and M. G. Thompson, Temperature Dependence of the Kerr Nonlinearity and Two-Photon Absorption in a Silicon Waveguide at 1.55μm, Phys. Rev. Appl. **11**, 044084 (2019).

[2] W. Sohler, H. Hu, R. Ricken, V. Quiring, C. Vannahme, H. Herrmann, D. Büchter, S. Reza, W. Grundkötter, S. Orlov, H. Suche, R. Nouroozi, and Y. Min, Integrated optical devices in lithium niobate, Opt. Photon. News **19**, 24 (2008).

[3] Y.-S. Lee, T. Meade, M. DeCamp, T. Norris, and A. Galvanauskas, Temperature dependence of narrow-band terahertz generation from periodically poled lithium niobate, Appl. Phys. Lett. **77**, 1244 (2000).

[4] S. Carbajo, J. Schulte, X. Wu, K. Ravi, D. N. Schimpf, and F. X. Kärtner, Efficient narrowband terahertz generation in cryogenically cooled periodically poled lithium niobate, Opt. Lett. **40**, 5762 (2015).

[5] K. J. Satzinger, Y. Zhong, H.-S. Chang, G. A. Peairs, A. Bienfait, M.-H. Chou, A. Cleland, C. R. Conner, É. Dumur, J. Grebel, *et al.*, Quantum control of surface acoustic-wave phonons, Nature **563**, 661 (2018).

[6] A. Youssefi, I. Shomroni, Y. J. Joshi, N. Bernier, A. Lukashchuk, P. Uhrich, L. Qiu, and T. J. Kippenberg, Cryogenic electro-optic interconnect for superconducting devices, arXiv:2004.04705 (2020).

[7] J. D. Morse, K. G. McCammon, C. F. McConaghy, D. A. Masquelier, H. E. Garrett, and M. E. Lowry, in *Design, Simulation, and Fabrication of Optoelectronic Devices and Circuits* (International Society for Optics and Photonics, Los Angeles, 1994), Vol. 2150, p. 283.

[8] C. McConaghy, M. Lowry, R. A. Becker, and B. E. Kincaid, The performance of pigtailed annealed proton exchange $LiNbO_3$ modulators at cryogenic temperatures, IEEE Photonics Technol. Lett. **8**, 1480 (1996).

[9] C. Herzog, G. Poberaj, and P. Günter, Electro-optic behavior of lithium niobate at cryogenic temperatures, Opt. Commun. **281**, 793 (2008).

[10] S. L. Bravina, A. N. Morozovska, N. V. Morozovsky, and Y. A. Skryshevsky, Low-temperature pyroelectric phenomena in lithium niobate single crystals, Ferroelectrics **298**, 31 (2004).

[11] X. Wu, C. Zhou, W. R. Huang, F. Ahr, and F. X. Kärtner, Temperature dependent refractive index and absorption coefficient of congruent lithium niobate crystals in the terahertz range, Opt. Express **23**, 29729 (2015).

[12] F. Thiele, F. vom Bruch, V. Quiring, R. Ricken, H. Herrmann, C. Eigner, C. Silberhorn, and T. J. Bartley, Cryogenic electro-optic polarisation conversion in titanium in-diffused lithium niobate waveguides, Opt. Express **28**, 28961 (2020).

[13] P. R. Sharapova, K. H. Luo, H. Herrmann, M. Reichelt, T. Meier, and C. Silberhorn, Toolbox for the design of $LiNbO_3$-based passive and active integrated quantum circuits, New J. Phys. **19**, 123009 (2017).

[14] N. Montaut, L. Sansoni, E. Meyer-Scott, R. Ricken, V. Quiring, H. Herrmann, and C. Silberhorn, High-Efficiency Plug-and-Play Source of Heralded Single Photons, Phys. Rev. Appl. **8**, 024021 (2017).

[15] J. P. Höpker, T. Gerrits, A. Lita, S. Krapick, H. Herrmann, R. Ricken, V. Quiring, R. Mirin, S. W. Nam, C. Silberhorn *et al.*, Integrated transition edge sensors on titanium in-diffused lithium niobate waveguides, APL Photonics **4**, 056103 (2019).

[16] R. W. Boyd, *Nonlinear Optics* (Academic Press, New York, 2008), 3rd ed.

[17] G. Edwards and M. Lawrence, A temperature-dependent dispersion equation for congruently grown lithium niobate, Opt. Quantum Electron. **16**, 373 (1984).

[18] D. H. Jundt, Temperature-dependent Sellmeier equation for the index of refraction, n_e, in congruent lithium niobate, Opt. Lett. **22**, 1553 (1997).

[19] M. Yamada, N. Nada, M. Saitoh, and K. Watanabe, First-order quasi-phase matched $LiNbO_3$ waveguide periodically poled by applying an external field for efficient blue second-harmonic generation, Appl. Phys. Lett. **62**, 435 (1993).

[20] See the Supplemental Material at http://link.aps.org/supplemental/10.1103/PhysRevApplied.15.024028 for complementary data to Fig. 4 and video illustrations of the experimental data in Fig. 8.

[21] S. Helmfrid, G. Arvidsson, and J. Webjörn, Influence of various imperfections on the conversion efficiency of second-harmonic generation in quasi-phase-matching lithium niobate waveguides, JOSA B **10**, 222 (1993).

[22] M. Santandrea, PyNumericalPhasematching v1.0 (2019). doi:10.5281/zenodo.3538004.

[23] P. Virtanen *et al.*, SciPy 1.0: Fundamental algorithms for scientific computing in PYTHON, Nat. Methods **17**, 261 (2020).

[24] S. B. Lang, *Sourcebook of Pyroelectricity* (Gordon and Breach, New York, 1974).

[25] S. Jachalke, E. Mehner, H. Stöcker, J. Hanzig, M. Sonntag, T. Weigel, T. Leisegang, and D. Meyer, How to measure the pyroelectric coefficient? Appl. Phys. Rev. **4**, 021303 (2017).

[26] Y. V. Shaldin, V. Gabriélyan, and S. Matyjasik, Pyroelectric properties of real $LiNbO_3$ single crystals grown from a congruent melt, Crystallogr. Rep. **53**, 847 (2008).

[27] V. Gopalan and M. C. Gupta, Origin and characteristics of internal fields in $LiNbO_3$ crystals, Ferroelectrics **198**, 49 (1997).

[28] I. S. Akhmadullin, V. Golenishchev-Kutuzov, S. Migachev, and S. Mironov, Low-temperature electrical conductivity of congruent lithium niobate crystals, Phys. Solid State **40**, 1190 (1998).

[29] A. Dhar, N. Singh, R. K. Singh, and R. Singh, Low temperature dc electrical conduction in reduced lithium niobate single crystals, J. Phys. Chem. Solids **74**, 146 (2013).

[30] *RSoft FemSIM* (Synopsys, Inc., 20.8.2019).

[31] E. Strake, G. Bava, and I. Montrosset, Guided modes of Ti:$LiNbO_3$ channel waveguides: A novel quasi-analytical technique in comparison with the scalar finite-element method, J. Lightwave Technol. **6**, 1126 (1988).

[32] S. Korotky, W. Minford, L. Buhl, M. Divino, and R. Alferness, Mode size and method for estimating the propagation constant of single-mode Ti:$LiNbO_3$ strip waveguides, IEEE J. Quantum Electron. **18**, 1796 (1982).